Shock-induced collapse of surface nanobubbles

Journal Name

ARTICLE TYPE

Cite this: DOI: 00.0000/xxxxxxxxxx

Shock-induced collapse of surface nanobubbles†

Duncan Dockar,[a]* Livio Gibelli,[a] and Matthew K. Borg[a]

Received Date
Accepted Date

DOI: 00.0000/xxxxxxxxxx

The collapse of cavitation bubbles often releases high-speed liquid jets capable of surface damage, with applications in drug delivery, cancer treatment, and surface cleaning. Spherical cap-shaped surface nanobubbles have previously been found to exist on immersed substrates. Despite being known nucleation sites for cavitation, their collapsing dynamics are currently unexplored. Here, we use molecular dynamics simulations to model the shock-induced collapse of different surface nanobubble sizes and contact angles. Comparisons are made with additional collapsing spherical nanobubble simulations near a substrate, to investigate the differences in their jet formation and resulting substrate pitting damage. Our main finding is that the pitting damage in the surface nanobubble simulations is greatly reduced, when compared to the spherical nanobubbles, which is primarily caused by the weaker jets formed during their collapse. Furthermore, the pit depths for surface nanobubble collapse do not depend on bubble size, unlike in the spherical nanobubble cases, but instead depend only on their contact angle. We also find a linear scaling relationship for all bubble cases between the final substrate damage and the peak pressure impulse at the impact centre, which can now be exploited to assess the relative damage in other computational studies of collapsing bubbles. We anticipate the more controlled surface-damage features produced by surface nanobubble cavitation jets will open up new applications in advanced manufacturing, medicine, and precision cleaning.

1 Introduction

Cavitation is the phenomenon where bubbles can rapidly expand and collapse within a liquid in response to local pressure variations. The high-speed liquid jets that develop during cavitation bubble collapse are often considered responsible for the pitting and wear of turbomachinery.[1] However, the concentrated impacts of these jets can be utilised for beneficial applications at the nano and microscale, such as in ultrasonic cleaning,[2] wastewater treatment,[3] cancer diagnosis and therapy,[4,5] and enhanced drug and gene delivery via sonoporation.[6]

The collapsing dynamics of spherical micro/macro-scale bubbles have been investigated extensively through a variety of experimental and simulation techniques, which generally follow a similar process: the bubble deforms from sphericity while an internal liquid jet develops, usually towards a solid substrate, away from a free surface, and/or in the same direction as an incident shock-wave. In most cases, the jet pierces the bubble's far-side or "distal" surface, while the bubble reconnects to form a toroidal shape.[7–14] As the jet continues through the external liquid after re-entry, it can result in permanent damage upon impact with a nearby solid surface.[9–11] The exact mechanism for the resulting damage is still not fully understood, however, different suggested explanations in the literature have included fatigue failure for repeated bubble collapses,[15] or impulsive pressures during jet impact and from complex shock-wave interactions.[1,9,16–18]

Spherical nanobubbles (see Figure 1(a)), however, typically do not exhibit jetting behaviour during spontaneous collapse under ambient pressure, which is due to the dominant effects of viscosity at reduced length-scales, even for low internal vapour densities.[19–22] Instead, shock-waves are often employed to induce this violent collapse in simulations,[22,24–30] which could arise from the collapse of nearby larger bubbles.[17] It has also been suggested that poration of the blood-brain barrier by shock-induced nanobubble collapse is one cause of mild traumatic brain injury, which adds further motive to understanding their damage capacity.[24,31]

Bubble collapse near a wall is often characterised in terms of the stand-off parameter $\chi = z_c/R$, where z_c is the perpendicular distance from the wall to the centre of the bubble and R is the maximum radius of curvature before collapse.[8,11] Generally, micro/macro-scale bubbles with a lower stand-off height during spontaneous collapse, result in greater pit damage.[11] However, the effect of stand-off is not obvious during shock-induced col-

[a] School of Engineering, Institute of Multiscale Thermofluids, The University of Edinburgh, Edinburgh EH9 3FB, UK

*E-mail: d.dockar@ed.ac.uk

† Electronic supplementary information (ESI) available: Three supplementary movies and a PDF document of measurement techniques and discussions on associated errors. See DOI: 00.0000/00000000

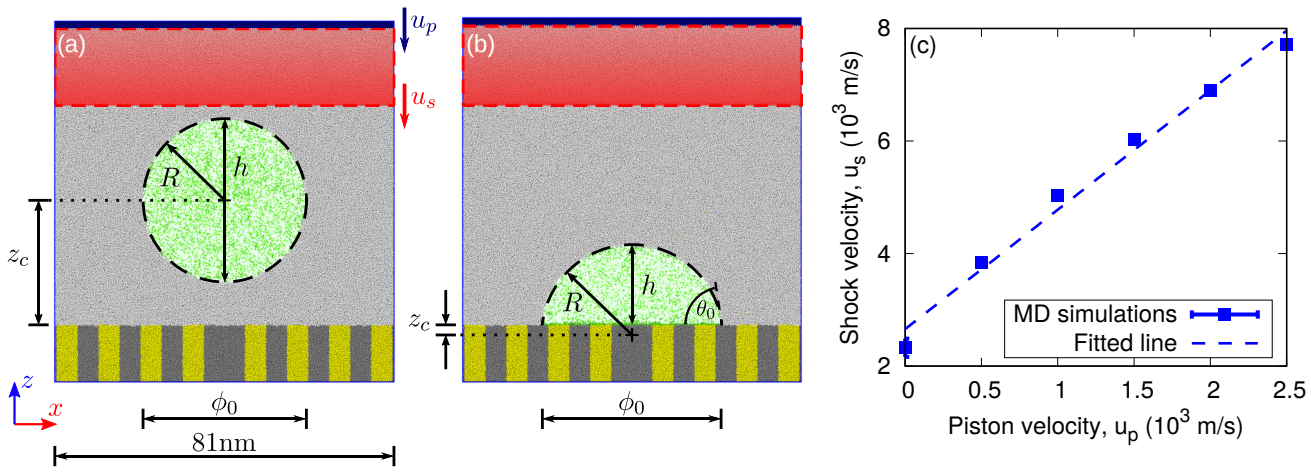

Fig. 1 Schematics of the molecular dynamics (MD) simulation set-up for the 40 nm diameter: (a) spherical, and (b) high contact angle (HCA) surface nanobubble cases. The mW water molecules are shown in light-grey, mN nitrogen molecules in green, piston atoms in dark-blue, and hydrophobic (aSi_o) and hydrophilic (aSi_i) atom types in yellow and dark-grey, respectively.[23] The renderings show a thin slice through the centre of the 3D MD simulations. The red highlighted region shows the propagation of the shock-wave with velocity u_s, driven by the piston at velocity u_p. (c) Variation in measured shock-wave velocity u_s, with piston velocity u_p, in the mW model. The dashed line shows the linear fit, as given in Equation (3).

lapse due to the complex interference of shock-waves and reflections, with peak substrate pressures and damage having been observed for $\chi \approx 1.3$–2 in simulations.[16,27,28]

Surface nanobubbles (see Figure 1(b)) are nanoscale gaseous domains that rest on solid surfaces, which can exist in stable diffusive equilibrium with lifetimes of up to several days and even weeks.[32–40] It has been previously suggested that these surface nanobubbles act as nucleation sites for cavitation, which has long been known to preferentially occur on solid surfaces and impurities.[39,41–43] Due to their spherical cap shape and pinned three-phase contact line, they have been shown to resist pressures many mega-Pascals lower than the classical Blake threshold for unstable growth,[42] and have also been found to oscillate with higher natural frequencies than spherical bubbles.[44]

The existence of surface nanobubbles has been the subject of recent debate, with the generally accepted mechanism for their diffusive stability reliant on contact line pinning (by chemically patterned or rough hydrophobic surfaces) and a supersaturated liquid,[36,45–47] although other studies have provided evidence for surface nanobubble stability without such contact line pinning.[48–50] While not a lot is known surrounding the novel stability mechanism of these unpinned nanobubbles, this discovery could possibly permit the existence of long-lived bulk nanobubbles, which has also seen increased interest in recent years.[51–53] Bulk and surface nanobubbles could be particularly attractive for the proposed cavitation technologies mentioned above, since their long proposed lifetimes may allow them to store chemicals/agents in the gas phase that could enhance their efficacy in both medical treatment and jet impact.[3,6,54] Surface nanobubble collapse has also speculated to be the cause of increased pitting on hydrophobic regions of substrates subjected to ultrasonic irradiation.[43]

Despite their theoretical interest and practical importance, the collapsing dynamics of surface nanobubbles have not yet been investigated. In this paper, we model the shock-induced collapse of surface nanobubbles using three-dimensional (3D) Molecular Dynamics (MD) simulations, capturing both the fluid and solid response, which would otherwise require complex multi-physics computation.[15,55,56] We also make comparisons to spherical nanobubble simulations, highlighting the differences in jet development, and resulting substrate damage.

2 Molecular Dynamics Simulations

We performed simulations using the Large-scale Atomic/Molecular Massively Parallel Simulator (LAMMPS) MD software,[57] employing the monatomic water (mW),[58] monatomic nitrogen (mN),[59] and amorphous silicon (aSi)[60] models for the liquid, gas and solid phases, respectively. Water and nitrogen were specifically chosen, given this is a common fluid combination for nanobubble studies.[39,40] Our MD set-up is made up of approximately 17 M water molecules per simulation, with an additional 800–85 k nitrogen molecules, depending on the simulation case. The amorphous silicon substrate was composed of 4.2 M atoms, with a thickness of 13 nm, and was patterned with alternating concentric rings of aSi_i and aSi_o atom types, with equilibrium (gas-side) contact angles of 88° and 37°, respectively.§ The substrate patterning provided pinning sites for the three-phase contact line,[61] which also allowed us to easily equilibrate a range of contact angles, for a particular size. In the Introduction, we discussed the possibility of diffusively stable surface nanobubbles without contact line pinning,[48,49] although, there has been no definitive description of this stability mechanism. Therefore, we base our current set-up on the currently accepted contact line pinning (and supersaturation) criterion, by use of concentric ring pinning sites.[36,39,40,45,46] The aSi_o substrate would appear to form a so-called "superhydrophobic"

§ Contact angle is conventionally measured from the liquid side in the literature, however, we will be using the gas-side contact angle for our discussions on surface nanobubbles.

material, which we found was necessary to equilibrate the low contact angle surface nanobubble cases that we investigate here, with contact angles of around 40°. In our simulations, we chose to model an initially atomically smooth substrate to better evaluate the pitting damage after bubble collapse, which prevented us from pinning the contact line with structural roughness. For this approach, we justify the use of our superhydrophobic aSi_o atoms for stabilising the 40° low contact angle surface nanobubbles, which have been commonly reported in experiments.[39,40]

The bulk mW and aSi interactions were modelled using the Stillinger-Weber (SW) potential, given by:

$$U_{SW} = \sum_i \sum_{j>i} A_s \varepsilon_{ij} \left[B_s \left(\frac{\sigma_{ij}}{r_{ij}} \right)^{p_s} - \left(\frac{\sigma_{ij}}{r_{ij}} \right)^{q_s} \right] \times \exp\left(\frac{\sigma_{ij}}{r_{ij} - a_s \sigma_{ij}} \right) + \sum_i \sum_{j \neq i} \sum_{k>j} \lambda_s \varepsilon_{ij} \left[\cos\theta_{jik} - \cos\theta_s \right]^2 \times \exp\left(\frac{\gamma_s \sigma_{ij}}{r_{ij} - a_s \sigma_{ij}} \right) \exp\left(\frac{\gamma_s \sigma_{ik}}{r_{ik} - a_s \sigma_{ik}} \right), \quad (1)$$

where U_{SW} is the total potential energy between the system of atoms/molecules interacting by the SW potential.[57,62] Atoms i and j are separated by distance r_{ij}, and likewise, i and k are separated by r_{ik}; atoms j and k form an angle θ_{jik} subtended at atom i. Specific material properties were achieved with the fitting parameters A_s, B_s, a_s, p_s, q_s, λ_s, θ_s, γ_s and are given for the mW and aSi models in Table 1. Potential parameters ε and σ are the characteristic potential depth and length-scale, respectively, between pairs of atoms as defined by their subscripts, and are given in Table 2. Interaction potentials between the hydrophobic and hydrophilic aSi atoms were identical.

Table 1 Fitting parameters used in Equation (1) to obtain intramolecular models for monatomic water (mW) and amorphous silicon (aSi)

Fitting parameter	mW[a]	aSi[b]
A_s	7.049 556 27	7.049 556 27
B_s	0.602 224 558 4	0.602 224 558 4
a_s	1.8	1.8
p_s	4	4
q_s	0	0
λ_s	23.15	31.5
θ_s	109.47°	109.47°
γ_s	1.2	1.2

[a] Ref. 58 [b] Ref. 60

All other atomic interactions were modelled using the Lennard-Jones (LJ) potential:

$$U_{LJ} = \sum_i \sum_{j>i} 4\varepsilon_{ij} \left[\left(\frac{\sigma_{ij}}{r_{ij}} \right)^{12} - \left(\frac{\sigma_{ij}}{r_{ij}} \right)^{6} \right], \quad (2)$$

where U_{LJ} is the total potential energy from all the LJ potential interactions.[57] The potential parameters for all other interactions, along with atomic masses, are also given in Table 2.

Schematics of the 3D spherical and surface nanobubble MD simulations are shown in Figures 1(a) and (b), respectively. For each bubble type, four sizes were initialised, ranging from $\phi_0 =$ 20–50 nm, with the size ϕ_0 defined as the spherical bubble's diameter, or the surface nanobubble's lateral contact diameter. The aSi_o/aSi_i substrate patterning had 10 nm periodicity, and was ordered such that the hydrophobic atoms always formed a ring with outer diameter ϕ_0, to ensure pinning of the surface nanobubble's contact line. We also included the patterning in the spherical nanobubble simulations for consistency, which was not expected to have a strong effect on the collapse, although did prove useful in visualising the substrate damage (see Section 3.3).

Table 2 Atom types and parameters for interatomic potential interactions for the monatomic water (mW), monatomic nitrogen (mN), amorphous silicon (aSi) and piston (Ps) atoms

Atom/ Interatomic pair[a]	Atom Mass (g/mol)	ε (kJ/mol)	σ (nm)
mW[b]	18.015	25.895	0.23925
mW–mN[c]	-	0.41250	0.30713
mW–aSi_o	-	1.0534	0.22438
mW–aSi_i	-	1.9726	0.22438
mN[d]	28.013	0.79155	0.37500
mN–aSi_o	-	4.3008	0.27076
mN–aSi_i	-	2.3704	0.27076
aSi[e]	28.085	159.04	0.20951
Ps–mW[c]	-	1.8995	0.24318
Ps–mN[c]	-	2.3334	0.31105

[a] Parameters for atoms in bold are assumed for pairs of like atoms. Any interaction pairs not given are equal to zero.
[b] Ref. 58 [c] Ref. 44 [d] Ref. 59 [e] Ref. 60

For each size, we modelled two types of surface nanobubbles: a high contact angle (HCA) case initialised with $\theta_0 = 80°$, and a low contact angle (LCA) case with $\theta_0 = 40°$. These bubbles are equivalent to $\chi = -0.17$ and $\chi = -0.77$, respectively, when the stand-off parameter is expressed as $\chi = z_c/R = -\cos\theta_0$. Supersaturation in the respective initialised surface nanobubble states was applied to provide conditions for diffusive stability for the defined contact angles, as given in Ref. 36. Regardless, the micro-second timescales of diffusive growth effects were not expected to significantly influence the pico-second scales of these simulations.[1,36,39] We initialised the spherical nanobubble simulations with $\chi = 1.5$, in the range of expected peak substrate pressures.[16,27,28]

All cases were equilibrated for up to 0.5 ns, maintained at $T =$ 300 K with a Nosé–Hoover thermostat[57,63,64] and a fixed pressure $P_{\infty,0} = 0.1$ MPa by use of a piston (comprising of 6.22×10^5 atoms, and with a total mass of 2.01×10^{-19} kg), until they had reached mechanical stability.[42,44¶] Interatomic potential parameters for the piston (Ps) atoms are also given in Table 2. Periodic boundary conditions were applied in the x and y directions, with fixed boundaries in the z direction to prevent unintended periodic interactions with the piston and lower wall. The equilibrated fluid

¶ While this would not be enough time to reach diffusive stability, which was limited by the extreme computational cost of these simulations, this was long enough for the system to become mechanically stable, which we deemed sufficient, given the relatively short time-scale of the main production run.

domains had sizes of $81 \times 81 \times 82\,\mathrm{nm}^3$ in the x, y, and z directions, respectively, although were allowed to vary in the z direction to allow vertical displacement of the piston.

Three additional "vapour bubble" simulations were also carried out for the 40 nm bubbles, where all the gas molecules were removed immediately before shock-wave propagation to investigate the differences in vapour bubble collapse. Finally, a "no-bubble" case was simulated as a reference, with just the liquid and solid regions, to evaluate the plane shock-wave's effect on the substrate. Table 3 summarises all the MD cases modelled here, along with the final equilibrated bubble sizes.

Table 3 Different cases for the collapsing nanobubble MD simulations

Bubble case	Equilibrated size ϕ_0 (nm)	Equilibrated contact angle θ_0 (°)[a]
20 nm Spherical	17.7	–
20 nm HCA	23.2	84
20 nm LCA	22.1	40
30 nm Spherical	31.0	–
30 nm HCA	34.3	87
30 nm LCA	31.0	45
40 nm Spherical[b]	38.9	–
40 nm HCA[b]	44.0	83
40 nm LCA[b]	38.0	38
50 nm Spherical	53.9	–
50 nm HCA	53.9	77
50 nm LCA	52.8	40
No-bubble	–	–

[a] Applies only to the surface nanobubble cases.
[b] Cases in which an additional simulation was performed with nitrogen molecules removed before collapse, representing a vapour bubble.

During the main production runs, a shock-wave was propagated towards the bubbles by moving the piston downwards with constant speed $u_p = 2500\,\mathrm{m/s}$ (equivalent to Mach number $Ma = 1.07$ in water using the mW model) for 4 ps, after which, the piston was then set to reapply the 0.1 MPa pressure for the remainder of the simulations, up to 35 ps. These parameters were found from preliminary simulations to induce jetting for the range of bubble sizes investigated here, and were comparable to previous MD simulations.[22,24–26,28] The shock-wave travelled with speed $u_s = 7800\,\mathrm{m/s}$, and the pressure jump across the shock front was measured to be approximately $19.45(\pm 0.03)$GPa (see Figure S1 in the Electronic supplementary information (ESI)[†]). This pressure is very close in magnitude to that estimated by $\rho_0 u_s u_p = 19.5\,\mathrm{GPa}$, where the equilibrium liquid density is $\rho_0 = 1000\,\mathrm{kg/m^3}$.[25,65,66] No thermostat was applied to the fluid molecules during the main run, but was applied to the amorphous silicon to maintain the temperature at 300 K, with the bottom layer of solid atoms kept rigid to prevent displacement of the wall from the impinging shock-waves.

Figure 1(c) shows the relationship between piston velocity and shock-wave velocity in the mW liquid, found from several smaller no-bubble cases. We include another data point at $u_p = 0\,\mathrm{m/s}$, equivalent to the speed of sound in the liquid phase $c_{0,l}$, which was approximated from $c_{0,l} = \sqrt{(\partial P/\partial \rho_0)_S} = 2300\,\mathrm{m/s}$, and using the equation of state from equilibrium simulations at various densities, where subscript S denotes at constant entropy. The shock-wave speed can be estimated by a linear fit:

$$u_s = c_{0,l} + \zeta u_p, \tag{3}$$

as shown in Figure 1(c),[||] where the fitted slope $\zeta = 2.1$ is consistent with experimental measurements and other MD water models.[26,66,67] Although, it is worth noting that the speed of sound of the mW model is greater than the experimental value of 1501.5 m/s at ambient pressure and temperature.[68]

We obtained material properties of the amorphous silicon model using tensile testing pre-simulations (thermostatted at 300 K), namely, the equilibrium density $\rho_s = 2200\,\mathrm{kg/m^3}$, and elastic modulus $E = 58.2\,\mathrm{GPa}$, which we used to estimate the speed of sound in the solid: $c_{0,s} = \sqrt{E/\rho_s} = 5160\,\mathrm{m/s}$.[69] We also measured the ultimate tensile strength and Poisson's ratio to be 5.5 GPa and $\nu_P = 0.328$, respectively.

3 Results and Discussion

3.1 Collapsing bubble and jet formation

All the bubble cases exhibited the typical jet formation upon collapse,[8–10,12,13] as shown in Figure 2 for the 40 nm cases. In the spherical cases, the jets first impacted the distal bubble surface, and then the substrate soon after, as can be seen in Figures 2(a)–(l). A toroidal rebounding bubble formed in the 40 nm and 50 nm spherical cases after the substrate impact, which can also be seen in Figure 2(l), although with a high internal density.

In the HCA surface nanobubble simulations (see 40 nm case in Figures 2(m)–(r)), the jets did not appear to fully develop before they had already impacted the substrate, since the top surfaces of the bubbles were already much closer to the substrate than for the spherical cases. This jetting effect was even less pronounced in the LCA cases, as shown in Figures 2(s)–(x), and with this inhibited jet formation, there was visibly less damage to the solid substrate compared to the spherical cases. There was also less outward flow from the impact centre, and no rebounding bubbles observed. Most of the nitrogen molecules remained dissolved, with a high gas concentration near the substrate, whereas in the spherical cases, the nitrogen molecules flowed away from the substrate, while forming the rebounding bubble. Animations of the MD simulation bubble collapses can be found in the ESI for each of the 40 nm cases.[†] All cases demonstrated cylindrical symmetry around the impact centre, and spatial results were binned accordingly, with bin sizes of $1 \times 1\,\mathrm{nm}^2$ in the z and r dimensions.

We tracked the bubble and solid interfaces from the 50 % isodensity contours, allowing us to measure the deformation of the bubble and substrate, which can also be seen by the solid black lines in Figure 2. The volumes of the bubbles V as they collapsed are shown in Figures 3(a), (b), and (c), for the spherical, HCA, and LCA cases, respectively, and are normalised by the maximum bubble volume just before collapse V_0. We define the

[||] Least-squares fitting was performed here, and for all other linear fitting procedures in this article.

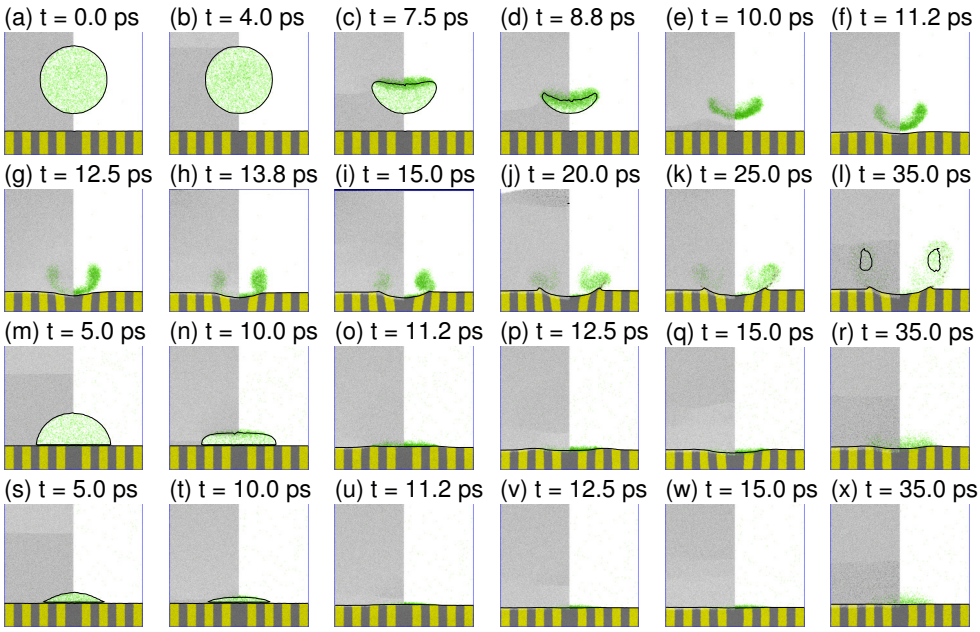

Fig. 2 Visualisations of the collapse of the gas-filled 40 nm diameter bubble cases: (a)–(l) spherical nanobubble; (m)–(r) HCA surface nanobubble; (s)–(x) LCA surface nanobubble. The timestamp is given for each subfigure. The mW water molecules are shown in light-grey, mN nitrogen molecules in green, and aSi_o and aSi_i atom types in yellow and dark-grey, respectively.[23] The renderings show a thin slice through the centre of the 3D MD simulations, with the 50% iso-density contours of the liquid-gas and solid-liquid interfaces shown overlaid as solid black lines, where present. The water molecules on the right-hand side of each image are not shown to improve the view of the bubble.

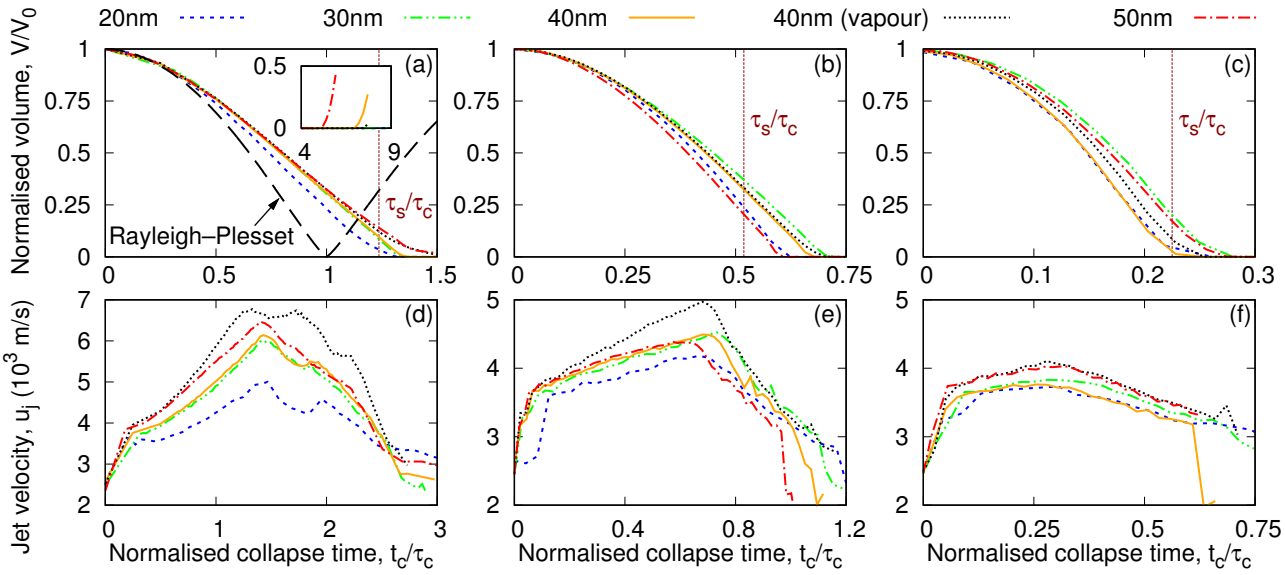

Fig. 3 Variation of normalised bubble volume V/V_0, with normalised time t_c/τ_c for the: (a) spherical nanobubble, (b) HCA, and (c) LCA surface nanobubble cases; the inset in (a) shows the formation of the rebounding toroidal bubbles in the 40 nm and 50 nm diameter spherical cases, by the end of the simulations. The normalised time taken for the shock-wave to move the length of the bubble τ_s/τ_c (see Equation (6)) is also shown for each bubble type. Variation of jet velocity u_j with normalised time t_c/τ_c for the: (d) spherical nanobubble, (e) HCA, and (f) LCA surface nanobubble cases.

collapse time t_c from when the shock-wave first reached the bubble, which was then normalised by the Rayleigh collapse time (see Equation (5) below), using the equilibrium density of water, $\rho_0 = 1000\,\mathrm{kg/m^3}$, measured shock-wave pressure $P_\infty = 19.45\,\mathrm{GPa}$ (from the no-bubble case), and negligible vapour pressure P_v at 300 K.[8,68,70]

Bubble cavitation dynamics are usually modelled by the Rayleigh–Plesset equation:[1,70,71]

$$R\ddot{R} + \frac{3}{2}\dot{R}^2 + \frac{4\mu}{\rho_0 R}\dot{R} = \frac{1}{\rho_0}\left[P_{g,0}\left(\frac{R_0}{R}\right)^{3k} - (P_\infty - P_v) - \frac{2\gamma}{R}\right], \quad (4)$$

where μ is the liquid dynamic viscosity, R is the radius of the bubble as a function of time, with initial radius R_0, $P_{g,0}$ is the initial gas pressure, γ is the liquid–gas surface tension, and k is

the exponent of the polytropic gas law (*i.e.* $P_g V^k = \text{const.}$). Dot notation is used to indicate time-derivatives, *e.g.* $\dot{R} = \mathrm{d}R/\mathrm{d}t$, and $\ddot{R} = \mathrm{d}^2R/\mathrm{d}t^2$. Equation (4) has been shown to correctly predict the spontaneous collapse of spherical vapour nanobubbles,[19,20] however, as mentioned previously, no jetting nor permanent damage were observed due to the dominant viscous forces.[22]

By assuming negligible contributions from viscosity, surface tension, and internal gas pressure, and by setting $\dot{R}(0) = 0$, Equation (4) can be solved analytically to obtain the Rayleigh collapse time:[70]

$$\tau_c = 0.4573\phi_0\sqrt{\frac{\rho_0}{(P_\infty - P_v)}}. \tag{5}$$

While Equation (5) is not strictly applicable for shock-wave induced collapse, we employ it here to demonstrate that the nanobubbles collapsed at similar rates, depending on their type, and we can compare these nanobubble collapsing dynamics to that of larger macroscale bubbles.

The collapse times for all the spherical bubbles exceeded the Rayleigh collapse time, although this is common for shock-induced collapse, and is due to the non-symmetric pressure distribution surrounding the bubble caused by the shock-wave, as well as the non-spherical collapse exhibited during jetting.[16,25,29,56,72] To verify this statement, we used Equation (4) to model the collapse of the 40 nm spherical nanobubble, as shown by the dashed black line in Figure 3(a), where $P_{g,0} = P_{\infty,0} + 2\gamma/R_0$ (as defined in our MD simulation set-up), and using fluid properties of the mW liquid model, $\mu = 3.550 \times 10^{-4}$ Pa s and $\gamma = 65.384$ mJ/m^2.[44] However, we find the viscosity and surface tension have negligible effects compared to the high shock-wave pressure, and the Rayleigh–Plesset solution predicts an almost exact collapse time as Equation (5), which confirms the shock-wave is responsible for the differences in the nanobubble collapse rates. Even the 40 nm vapour nanobubbles collapses were comparable to the respective gas-filled cases, which further confirms that it was not the high internal gas pressure that slowed down their collapse. Equation (4) also predicts an immediate rebound after collapse, due to the internal gas pressure, while our spherical nanobubble simulations undergo a complete collapse followed by a delayed rebound, as shown inset in Figure 3(a), which we speculate to be caused by the lasting fluid vorticity, as will be discussed later. We can see that Equation (5) overpredicts the collapse times for the HCA and LCA surface nanobubbles as well, in Figures 3(b) and (c), respectively.

The discussion above clearly shows that Equations (4) and (5) are unsuitable for predicting the shock-induced collapse in these nanobubble simulations. Even models such as the Keller-Miksis equation,[73] which account for liquid compressibility in cavitation bubble dynamics, would be unable to model for this type of shock-induced collapse, as they assume a spherically symmetric pressure distribution. While several corrections to Equation (5) have been previously applied for more complex drivers of collapse, such as the enhanced pressure upon shock-wave reflection with a nearby wall,[56] these modifications typically assume that the collapsing rate of the bubble is much longer than the propagation of the shock-wave. Therefore in those cases, the bubble would fully collapse some time after the shock-wave has passed the bubble. However, the bubbles cannot collapse faster than the rate at which the driving pressure increases, which is limited by the time taken for the shock-wave to pass the length of the bubble $\tau_s = h/u_s$, where h is the bubble height, measured from the travelling direction of the shock-wave.

By taking the ratio of the shock-wave propagation time τ_s to the Rayleigh collapse time τ_c, we obtain another estimate for the reduced collapse time:

$$\frac{\tau_s}{\tau_c} = \frac{h}{0.4573\phi_0 u_s}\sqrt{\frac{(P_\infty - P_v)}{\rho_0}}, \tag{6}$$

where $h = \phi_0$ for the spherical nanobubbles, or $h = \phi_0(1-\cos\theta)/2\sin\theta$ for the surface nanobubbles, as shown in Figures 1(a) and (b), respectively. Here, Equation (6) is actually independent of bubble size (since $h \propto \phi_0$), and depends only on the contact angle for the surface nanobubbles. Equation (6) predicts reduced collapse times of 1.24, 0.519, and 0.225, for the spherical, HCA, and LCA, nanobubble cases, respectively, which is in better agreement with our simulations, as shown in Figure 3(a)–(c). The actual collapse times took slightly longer than these estimates, due to liquid inertial effects during the jet development and partial deceleration of the shock-wave as it first impacted the bubble.

Further examination of Equation (6) also reveals the limit of piston velocity at which we expect Equation (5) to hold, which is satisfied when the shock-wave propagation time is much smaller than the predicted Rayleigh collapse time, *i.e.* $\tau_s \ll \tau_c$. By assuming that the internal vapour pressure P_v is negligible, the shock speed as given by Equation (3), and the pressure of the shock wave estimated by $P_\infty = \rho_0 u_p u_s$, we can rearrange Equation (6) to obtain $Ma < \left[1/0.4573^2 - \zeta\right]^{-1}$, where the Mach number is given by $Ma = u_p/c_{0,l}$. The right-hand side of this expression is equal to 0.37, for $\zeta = 2.1$ (in water), equivalent to a shock-wave pressure of $P_\infty \sim 1$ GPa. It would appear, then, that Equation (5) is unsuitable for predicting shock-induced nanobubble collapse, particularly when $Ma \sim 1$ piston velocities and ~ 10 GPa shock-wave pressures are generally used.[25,28–30] Instead, we propose estimating the collapse via the shock-wave propagation time: $\tau_s = h/u_s$.

We monitored the liquid jet by tracking the 50% iso-momentum density (ρu_j) contour within the fluid, where u_j is the jet velocity, as measured by the z velocity component towards the wall (see the ESI for more information[†]). The jet velocities also developed at similar rates, depending on the bubble type, as shown in Figure 3(d)–(f). All the jet velocities started around 2500 m/s (similar to the piston speed), and increased until they reached a peak, which corresponded to the first jet impact. This was either at the distal bubble surface for the spherical cases (Figure 3(d)), or at the solid substrate for the HCA and LCA surface nanobubbles (Figures 3(e), (f)). For the gas-filled spherical bubbles, the peak jet velocities roughly increased with size, although this relationship was less strong for the HCA and LCA surface nanobubble cases, which had similar jet velocities at impact. The jets from the vapour bubbles developed higher velocities than their respective equally-sized gas-filled bubbles, due to the lower internal density that minimised the liquid deceleration.

The jets began decelerating after the first impact in all cases. In the spherical cases, the jet continued through the lower liquid layer before its second impact on the solid substrate around $t_c/\tau_c = 1.8$, and then finally dissipating,[11] as shown for the 40 nm case in Figures 4(a)–(f). After impact with the solid, the jet diverged and flowed radially outwards, following the local deformation it induced in the substrate, and then finally travelling upwards, away from the solid.

In contrast, the surface nanobubble jet velocities did not develop fully before they had already impacted the solid substrate, as shown by the lower peak velocities in Figures 3(e) and 4(g)–(l) for the 40 nm HCA case. Furthermore, the radial velocity after impact was also reduced, with the flatter solid deformation not facilitating the same outward fluid flow as in the spherical cases.

Figures 4(a)–(c) show how the spherical bubble jets narrowed after passing through the initialised bubble centre, and also developed a curved leading profile before substrate impact. However, in the spherical cap-shaped surface nanobubbles, the jet was not able to finalise its development by passing through the geometric spherical centre. Instead, we find that the substrate's early obstruction to the underdeveloped jet meant that the leading jet profiles were flatter and wider at impact, which had implications for the reflected shock-wave interactions, as is discussed later. Generally, the surface nanobubble jets developed and reflected more like a plane shock-wave, as can be seen in Figures 4(j)–(l), rather than the concentrated impact of the spherical nanobubble jets.

To further investigate the effect of the bubble's collapse on the resulting outward jet flow and rebounding bubble formation, we measure the vorticity, as given by:

$$\vec{\eta} = \vec{\nabla} \times \vec{u}, \tag{7}$$

where the dominant, azimuthal component reduces to $\eta_\varphi = \partial u_r/\partial z - \partial u_z/\partial r$. The vorticity evolution for the 40 nm spherical and HCA cases are shown in Figures 5(a)–(c) and (d)–(f), respectively. Vorticity developed towards the outer edges of the bubbles, as the liquid circulated during jet formation, and continued until the jet's impact against the substrate. In the spherical cases, this vorticity reached its maximum during the jet's initial development and narrowing (see Figure 5(a)), and persisted well after the jet impact, while also generating a counter-rotating vortex as the fluid flowed outwards across the substrate, as seen in Figures 5(b)–(c), which could have contributed to the solid pitting damage. The enduring vorticity within the fluid would also have promoted the toroidal rebounding bubble formation, as seen inset in Figure 3(a). In the HCA surface nanobubble case, however, the vorticity did not reach the same magnitude as in the spherical case, and also dissipated much quicker after jet impact, which we identify as the reason for the reduced outward flow and no rebounding bubble. The vorticity developed in the 40 nm LCA case was negligible, and is not shown here. Animations of the jet velocity and fluid vorticity across the bubble during collapse can be found in the ESI for each of the 40 nm cases.[†]

3.2 Jet impact pressure

After each jet impact, high local fluid pressures were measured using the virial theorem (see the ESI for more information[†]) near the surface impact sites, which are caused by shock-wave reflections and interference,[65,66,74] as shown in Figures 6(a)–(l) and (m)–(x) for the 40 nm spherical and HCA cases, respectively. This increase in local pressure close to the substrate is often attributed as the main damage mechanism during cavitation, although the impulsive effects of these pressures should also be considered, as will be discussed later.[1,8,9,11,14,18,22,24] Animations of the pressure distributions across the bubble and substrate surfaces for each jet impact can be found in the ESI for each of the 40 nm cases.[†]

Figures 6(g)–(l) and (s)–(x) show the top-view of the pressure, taken from the cylindrically binned data at $z = 1$ nm (located just above the solid substrate), which we compare to the initial bubble diameter ϕ_0 from the white dashed circles, and final pit perimeter ϕ_d using solid black lines (the definition of ϕ_d is described in Section 3.3). Figures 6(b) and (h) show how the pressure first reached a concentrated maximum at the impact centre across the substrate, due to the spherical nanobubble's curved jet profile, which then advanced outwards (Figures 6(i)–(l)), while the jet diverged out across the substrate. Localised pressure peaks were also observed near the initial distal bubble surface height from the first jet impact, reaching almost 100 GPa, due to shock-wave interactions from reflections off the bubble surfaces, and augmented by the curvature of the impinging jet.[66] We see a very non-uniform pressure distribution following the jet impact in Figure 6(f), from the outward flow and subsequent toroidal rebounding bubble formation, and with low pressures observed around the outer edges of the developing pit, due to the nearby vorticity. We also noted previously how the forming pit shape redirected the jet velocity upwards in the spherical cases, with the increased rate of change in momentum also potentially contributing to the increased impact pressure.

In the surface nanobubble collapses, the flatter and wider jet profiles limited the localised effects of the reflected shock-wave interactions, and the pressure increase was more uniform across the jet diameter, as can be seen in Figures 6(p) and (v). Following the rapid jet dissipation, the impact pressures decayed quickly in the surface nanobubble cases, which is in contrast again to the spherical cases, where the jets diverged outwards across the substrate and maintained the impact pressure for longer. The fluid pressures during the latter stages of the surface nanobubble in Figure 6(r), more closely resembled a plane reflected shock-wave, like we saw in Figure 4(l).

Measured peak pressures after each jet impact P_j are presented for all bubble cases as a function of the incident jet velocity u_j in Figure 7. The incident shock-wave pressure (19.45 GPa) was subtracted from all results to show the pressure increase after impact. Furthermore, the pressure was averaged across the jet diameter to smoothen out the high pressure peaks at the impact centre, which can be up to three times the mean impact pressure.[66] Also shown in Figure 7 is the no-bubble case, with velocity equal to the piston velocity u_p, and pressure averaged across the whole plane

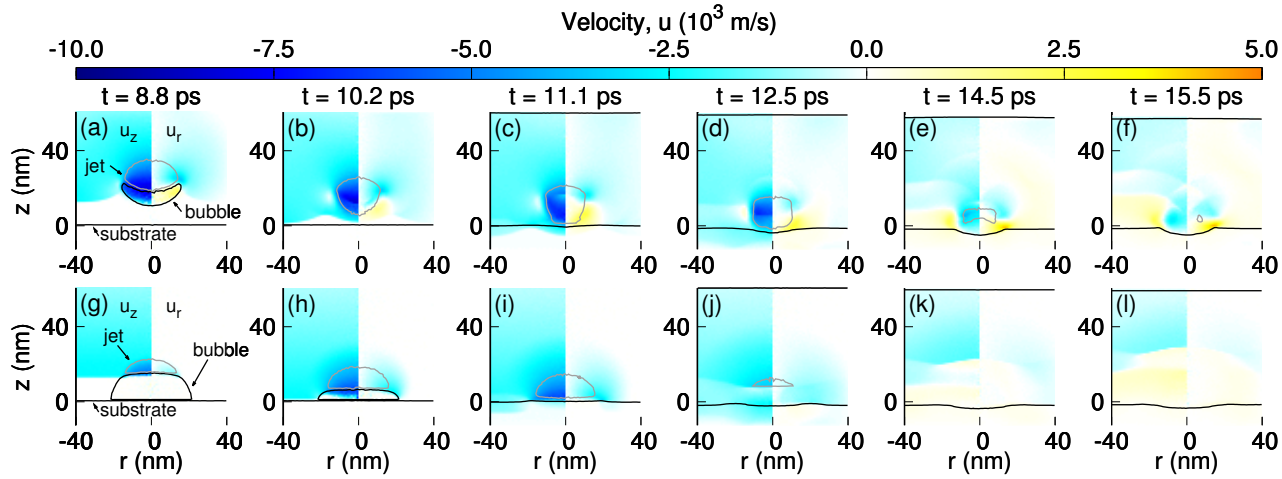

Fig. 4 Variation of fluid velocity and jet development in the 40 nm diameter: (a)–(f) spherical, and (g)–(l) HCA surface nanobubble simulations, in cylindrical coordinates, with the z axis defined through the centreline of impact, and r is the radial component from the centreline. Each plot is split in half at the centreline of the bubble impact: the left side shows the z component velocity, while the right side shows the r component velocity. The black lines show the bubble and substrate surfaces where present, and the dark-grey line shows the jet profile. The timestamps above (a)–(f) also apply to (g)–(l), respectively.

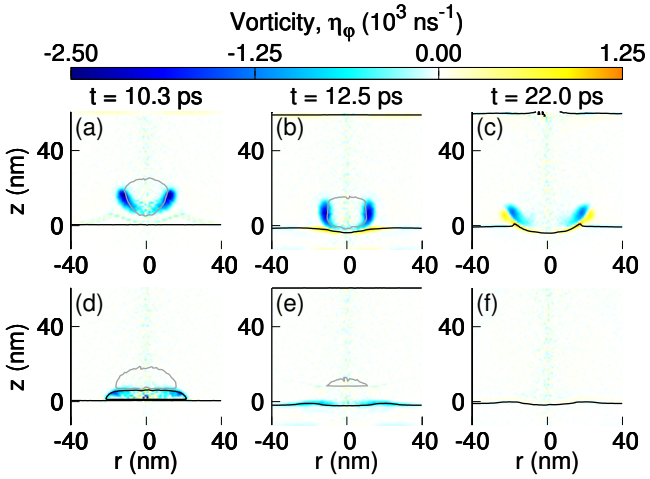

Fig. 5 Variation of fluid vorticity during jet development in the 40 nm diameter: (a)–(c) spherical, and (d)–(f) HCA surface nanobubble simulations, in cylindrical coordinates. Where present, the black lines show the bubble and substrate surfaces, and the dark-grey line shows the jet profile. The timestamps above (a)–(c) also apply to (d)–(f), respectively.

area. Despite the deceleration after the jet pierced through the distal surfaces of the spherical nanobubbles, the measured pressures were still relatively large for the substrate impacts, when compared with the surface nanobubble cases, which could have been enhanced by the increased shock-wave interactions from the preceding distal surface impact. For the spontaneous (non-shock induced) collapse of larger bubbles, which can be assumed mostly incompressible and with lower jet velocities,[8] the jet's second impact on the substrate has been shown to be weaker due to the deceleration through the lower liquid phase.[11]

We estimate the pressure from the impacting jets using the equation for water-hammer:[11,17,74]

$$P_{wh} = \rho_0 u_j c_{0,l} \frac{\rho_s c_{0,s}}{\rho_s c_{0,s} + \rho_0 c_{0,l}}, \tag{8}$$

which is strictly valid for low Mach number jet impact on a non-rigid substrate. Other shock-wave interactions from curved jet interfaces and higher Mach numbers also contribute to the impact pressure, as already observed in Figure 6.[66,74] Accounting for these additional effects is not trivial without full numerical simulation, however, we include comparisons to Equation (8) in Figure 7, to demonstrate that there is some expected relationship between jet velocity and impact pressure. Using equilibrium values for the amorphous silicon wall from Section 2, Equation (8) reduces to $P_{wh} \approx 0.83\rho_0 u_j c_{0,l}$, as shown by the straight line in Figure 8, and likewise, for the distal bubble surface impact, the liquid parameters (ρ_0, $c_{0,l}$) can be substituted instead of the respective solid parameters (ρ_s, $c_{0,s}$), and Equation (8) reduces to $P_{wh} \approx 0.5\rho_0 u_j c_{0,l}$,[16,17] as shown inset in Figure 7.

Equation (8) estimates the order of magnitude of the impact pressures, however, all the bubble cases were generally higher than the predicted water-hammer, due to these previously mentioned shock-wave effects. Generally, we would expect that the jet impact pressures increase from the LCA surface nanobubbles, HCA surface nanobubbles, and then the spherical nanobubbles, which follows from the inhibited jet development in the surface nanobubble cases. However, this trend is not so clear from the scattered data in Figure 7, due to the highly transient pressures arising from shock-wave reflections, as well as the statistical noise typically observed in MD simulations, which makes it difficult to use these measured peak pressures for quantifying damage. We will discuss the impulsive effects of these pressures later, which better reveal how the time-effects of the jet impact contribute to the substrate damage.

3.3 Pitting damage and impulse

Pitting damage was observed in all of the simulations, except for the no-bubble case, confirming that the bubble collapse was responsible for the pitting, and not just the result of an imping-

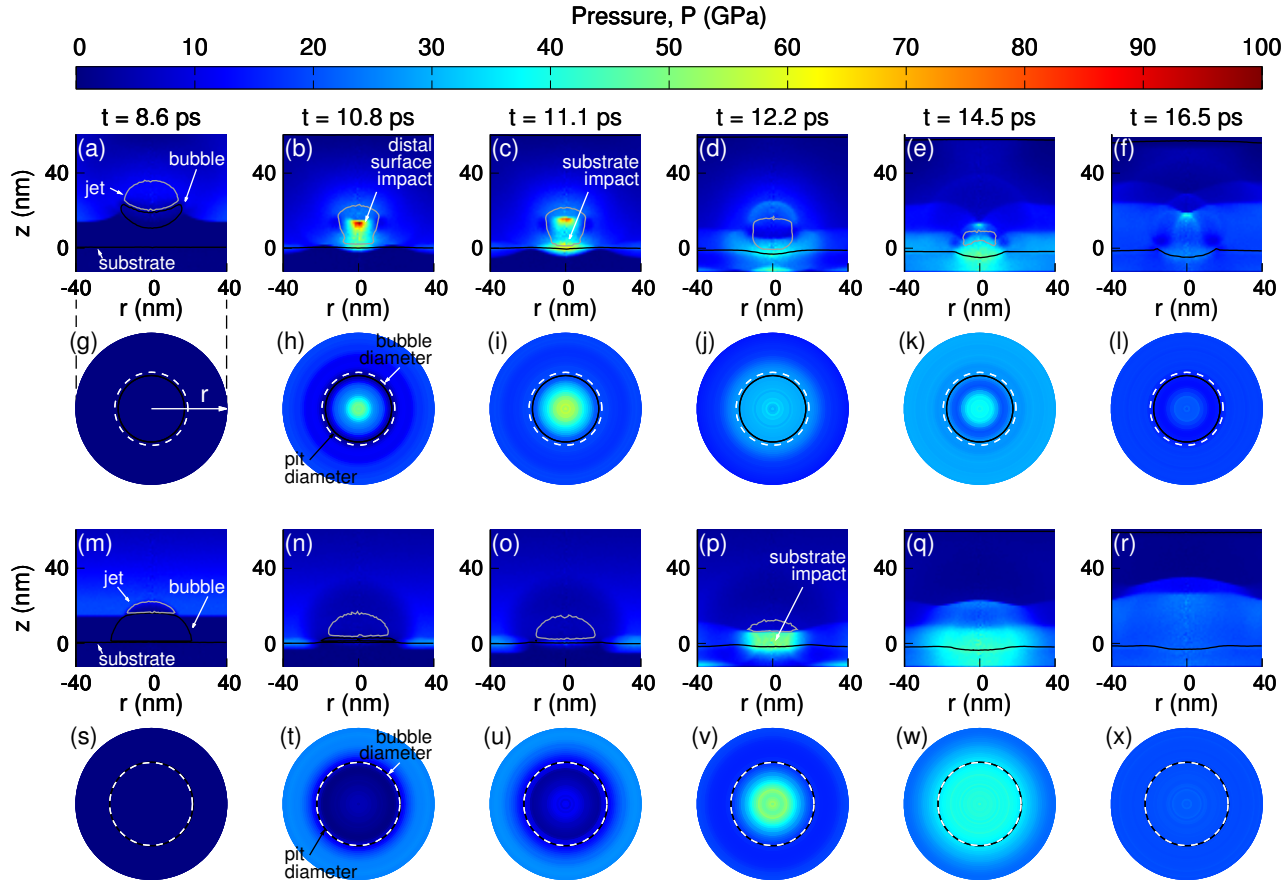

Fig. 6 (a)–(f) Side view variation in pressure in cylindrical coordinates for the 40 nm diameter spherical bubble collapse simulation; (g)–(l) top view variation in pressure, taken from the cylindrically binned data at $z = 1\,\text{nm}$ above the substrate. (m)–(r) Side view variation in pressure in cylindrical coordinates during 40 nm diameter HCA surface nanobubble collapse simulation; (s)–(x) top view variation in pressure, taken from the cylindrically binned data at $z = 1\,\text{nm}$ above the substrate. Where possible, the black lines show the bubble and substrate surfaces, and the dark-grey line shows the jet profile, in (a)–(f) and (m)–(r). The dashed white and solid black circles show the initial bubble and final pit diameters, respectively, in (g)–(l) and (s)–(x). The timestamps above (a)–(f) also apply to (g)–(l), (m)–(r) and (s)–(x), respectively.

ing shock-wave. For the spherical cases, the pits appeared to widen gradually during development, as the narrow curved jet profile first impacted the substrate and then diverged outwards, as shown in Figure 8(a) for the 40 nm case. We were able to fit a spherical cap shape to all the final pit profiles in these cases,[28,29] as can be seen by the dark-grey dashed line in Figure 8(a). There was a clear peak or "lip" formed around the perimeter, which as we mentioned earlier, helped direct the jet flow after impact. The surrounding substrate also deformed uniformly due to the shock-wave, although this was mostly recovered elastically by the end of the simulation.

Figure 8(b) shows the pit development for the 40 nm HCA surface nanobubble case, which ended with a flatter base and less sharp lip. The pit's width appeared roughly constant throughout its development, resulting from the preceding jet's flatter profile and more uniform impact pressure. Furthermore, the lack of outward jet flow and vorticity-driven shear stresses across the substrate produced lower curvature in the pit's interface, when compared to the spherical cases, and we were not able to fit a spherical cap shape to these pits.

The differences in pit shapes between the spherical and surface nanobubble cases arose from the jet's properties before impact. While the increased jet speed in the spherical cases had an expected increased effect on the impact pressure (see Figure 7), we also saw how the jet first impacted the substrate at a concentrated point, due to the jet's narrow diameter and high curvature, which then flowed radially out across the substrate, aided by the vorticity that was generated during the bubble's collapse, with displaced silicon atoms from the substrate forming a pit lip upon exit. We refer to this impact behaviour as "punch" and "drag", for the initial impact, and subsequent outward flow, respectively.

In contrast, the surface nanobubble jet impacted the substrate with lower jet velocity, a flatter and wider profile, and less vorticity generated, resulting in a similar, albeit wider, "punch" impact, but no outward flow or "drag". It is the dragging motion of the fluid across the substrate (from surface shear stresses) that is responsible for the spherical cap shaped pit with the sharp lip around the perimeter, which we can see in the spherical nanobubble case in Figure 8(a), but not in the HCA surface nanobubble case in Figure 8(b).

To quantitatively describe the pit damage for the different bubble cases, we define the pit diameter ϕ_d as the lateral diameter

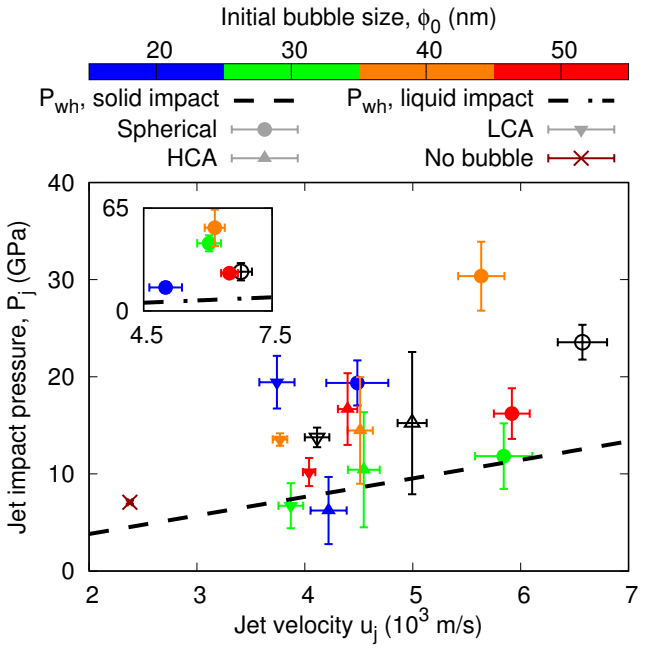

Fig. 7 Pressure increase immediately after each jet impact with the solid substrate versus incident jet velocity, for all cases. The inset shows the impact pressure for the jet impact on the distal bubble surface for the spherical cases. The straight lines show the predicted variation in water hammer pressure with jet velocity, from Equation (8), for the substrate and distal bubble surface impacts, shown as dashed and dot-dashed lines, respectively. The different symbols and colours denote the bubble type and size, respectively, as shown in the legend. The empty black symbols refer to the 40 nm diameter vapour bubble cases.

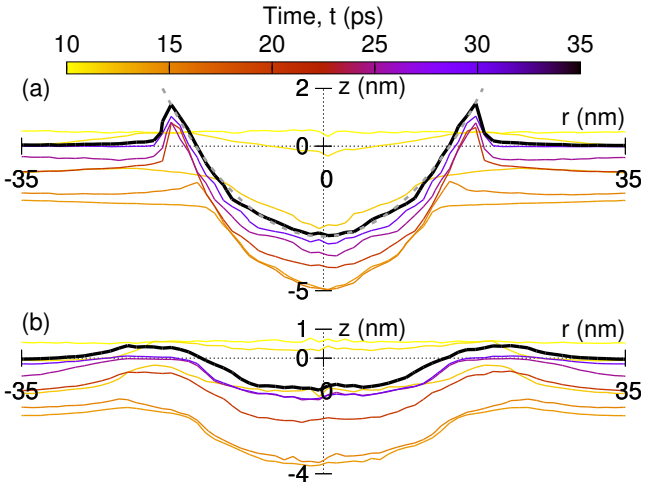

Fig. 8 Evolution of substrate pitting for the 40 nm diameter: (a) spherical nanobubble, and (b) HCA surface nanobubble cases. The colour of each line corresponds to the elapsed simulation time, as indicated by the legend, with the final pit shape shown by the bold black line. The dark-grey dashed line in (a) shows the spherical cap fit to the pit shape.

of the pit lip, as shown in the example schematic in Figure 9(a). The pit diameters were nearly identical to the initial bubble sizes ϕ_0, when compared to the $\phi_d = \phi_0$ dot-dashed line in Figure 9(e), and is consistent with previous investigations, which have empirically found that the final pit scales with initial bubble size in spherical bubble collapse.[11,28] Although the bubbles produced pits with similar perimeters, the depths d, defined by the vertical distance between the minimum pit level and the mean level of the undisturbed substrate $z_{Si,0}$ (see Figure 9(a)), varied significantly across bubble types, as shown in Figure 9(f). The spherical bubbles produced the deepest pits, which scaled linearly with bubble size, and we have fitted a zero-intercept straight line (for the gas-filled cases only), with a gradient of approximately 8.4 %, also shown in Figure 9(f). Interestingly, the pit depths from the surface nanobubble cases did not scale with the bubble sizes, and instead, we found that the pit depths from the HCA and LCA cases tended to around 1.2 nm and 0.23 nm (the latter being roughly the size of one water molecule), respectively, both shown as horizontal dotted lines. We would naturally expect this depth to tend to zero as ϕ_0 approached zero, although it is unclear if this constant pit depth would continue for larger surface nanobubbles. This phenomenon might make surface nanobubbles more suitable for applications involving delicate parts by mitigating damage from cavitation, however, repeated surface nanobubble collapses may still cause further damage by fatigue failure.[15]

Visually, the difference in surface damage between the spherical and surface nanobubble cases was also evident from the atomic debris, namely, the number of silicon atoms removed from the substrate by the end of the simulation. Figure 9(c) shows the aftermath of 40 nm spherical collapse, with approximately 9000 silicon atoms displaced. The sharp lip of the pit can be clearly seen, where the substrate deformed along the direction of the outward flow after the jet's substrate impact. In contrast, the 40 nm HCA surface nanobubble did not create as much atomic debris, only around 400 displaced atoms, which remained close the substrate by the end of the simulation, as shown in Figure 9(d).

Certain cavitation bubble dynamics, such as unstable growth and oscillatory behaviour, are characterised in terms of pressure,[1,42,44,75] however, in Section 3.2 we suggested that the impact pressure measurements would not be suitable for predicting damage, due to their highly transient nature from shock-wave interactions. Instead, it is the *impulse* that has been shown to be more important in quantifying collapsing behaviour, which is defined here as the time integral of pressure:[18,22,24,76]

$$I = \int_0^\infty P \mathrm{d}t, \tag{9}$$

where we measure pressure in the fluid plane at $z = 1$ nm (see Figures 6(g)–(l) and (s)–(x)). In doing so, we avoid the temporal statistical noise that obscured the previous pressure measurements, as in Figure 7, and also better capture the effects of the jet's prolonged impact duration in the spherical cases.

Equation (9) is closely related to the change in global fluid momentum per unit area,[14] and so with the same applied shock-wave formation, we would expect the same change in momentum, and therefore, approximately the same spatially averaged impulse in all our cases, in the absence of other external forces. However, Adhikari *et al.*[22] found that the measured impulse across a cell membrane during bubble collapse was actually *larger* for a smaller bubble, when using the same applied shock-wave parameters, and despite greater damage observed in the larger bubble case. Indeed, in our work, the mean impulse across the whole

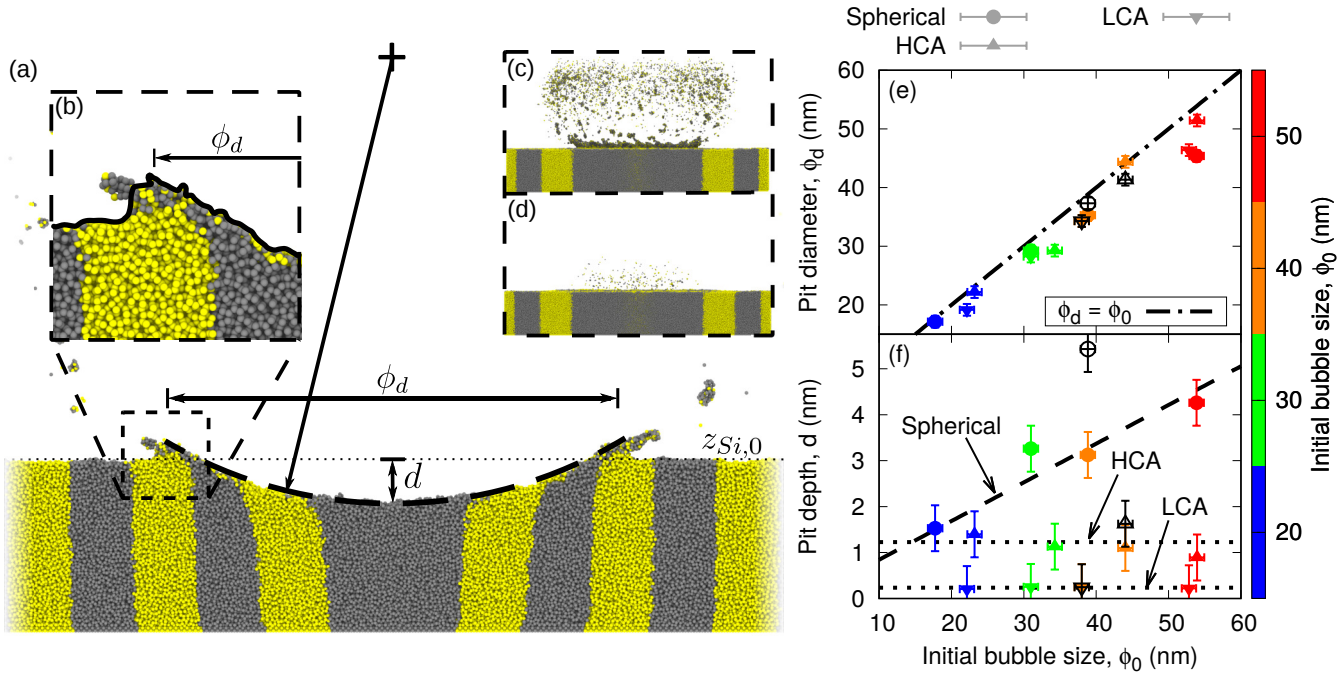

Fig. 9 (a) Schematic showing the typical solid substrate pitting damage (sliced view) at the end of the 40 nm diameter spherical bubble MD collapse simulation, with aSi_o and aSi_i atom types shown in yellow and dark-grey, respectively.[23] The dashed black line shows the fitted spherical cap shape to the pit (spherical cases only); the pit has lateral diameter ϕ_d and depth d. Inset (b) shows a closer view of the lip formed around the pit perimeter, and (c) and (d) show the full number of atomic debris released into the liquid for the 40 nm diameter spherical and HCA surface nanobubble cases, respectively. (e) Variation in the pit diameter with initial bubble diameter; and (f) variation in pit depth with initial bubble diameter, where the straight dashed line shows the line of best fit for the spherical cases, passing through the origin, and the horizontal dotted lines show the mean depths for the HCA and LCA cases, respectively. The different symbols and colours denote the bubble type and size, respectively, as shown in the legend. The empty black symbols refer to the 40 nm diameter vapour bubble cases.

substrate for each bubble case was less (up to 20%) than the no-bubble value of $I_0 = 257\,\text{mPa s}$, with the biggest deviations typically appearing in the larger (40–50 nm) spherical bubbles, which we believe is due to greater dissipation of fluid momentum by viscous stresses and solid deformation in these cases. Yet, we have already established in Figure 9(e) that the pit sizes increase with bubble diameter, which demonstrates that mean impulse alone cannot be used to quantify damage.

Instead, we plot the spatial impulse variation, measured radially from the impact centre with distance r, as shown in Figure 10 for all cases, where we see much more localised effects. The impulse distribution for the no-bubble case was approximately uniform, as expected for a plane shock-wave impact, and is shown as the flat line $I_0 = 257\,\text{mPa s}$. Similar impulse distribution shapes were observed depending on the bubble type, where the radial distance was normalised by half the initial bubble diameter ($\phi_0/2$). In Figure 10(a), the spherical cases all had a peak impulse at the impact centre, with some showing an intermediate trough around $2r/\phi_0 = 0.75$ before increasing again towards a steady value for $2r/\phi_0 > 1$. There were similar peak impulses at the impact centres in Figures 10(b) and (c) for the HCA and LCA surface nanobubble cases, respectively, which decreased to a steady value for $2r/\phi_0 > 1$. We note that the impulse never tended to the same mean impulse value of $I_0 = 257\,\text{mPa s}$ for large r, in any of the bubble cases. This occurs because the momentum of fluid away from the bubble is affected by the circulation during bubble collapse and jet formation, as shown in Figures 4 and 5, which would reduce the measured impulse in these regions.

Figure 10 shows how the impulse distribution varies depending on the bubble type and size, which is related to the jet's impact behaviour. We propose that the minimal damage caused by the no-bubble case, is mostly independent of the impulse magnitude, and instead, is purely due to the lack of a localised jet flow. For example, if another plane shock-wave/no-bubble case, was applied with mean impulse equal to $I = 385\,\text{mPa s}$, *i.e.* the maximum measured impulse from the 50 nm spherical bubble case, we would still expect no significant pitting damage, since no jet would be produced. Therefore, we suggest that it is the peak variation of impulse, or in other words, the ability of the bubble to redirect fluid momentum into a concentrated jet impact which is the most important feature for quantifying the bubble's damage capacity. We then plot the final pit volume (see Equation (10) below) against the peak impulse difference $\Delta I = I_{max} - I_0$ in Figure 11, where I_{max} is the peak impulse value at the impact centre for each bubble case.

We estimate the full damage of the silicon substrate at the end of the simulation by:

$$V_d = \int_0^\infty 2\pi r \left| z_{Si}(r) - z_{Si,0} \right| \mathrm{d}r, \tag{10}$$

where $z_{Si}(r)$ is the z coordinate of the silicon substrate's interface at a radial distance r, and $z_{Si,0}$ is the mean z height of the undis-

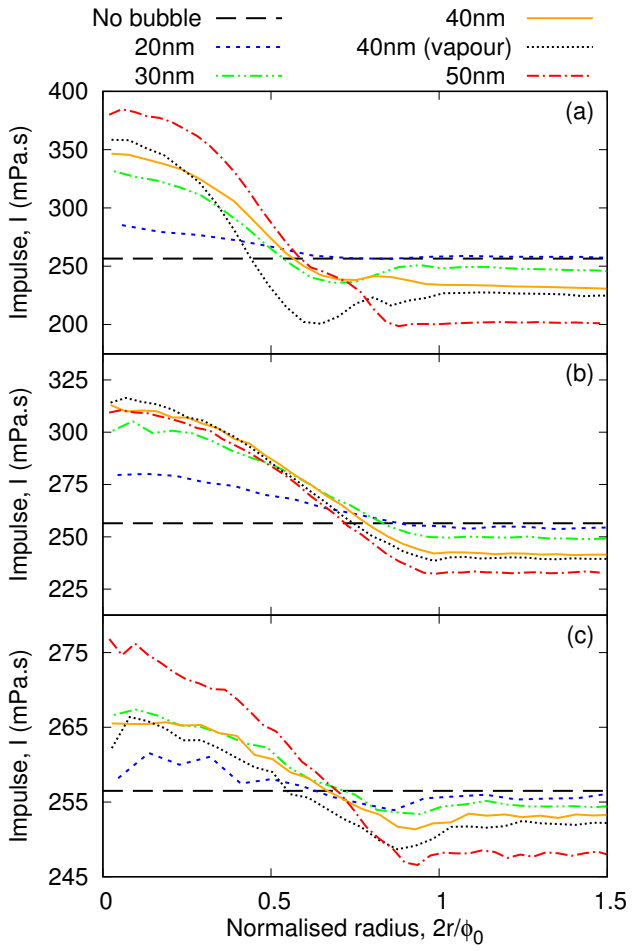

Fig. 10 Radial variation of the impulse distribution from the impact centre, as measured in the plane $z = 1\,\text{nm}$, after 35 ps, for the (a) spherical, (b) HCA, and (c) LCA nanobubble cases. Radial distance is normalised by half the initial bubble diameter, *i.e.* $\phi_0/2$.

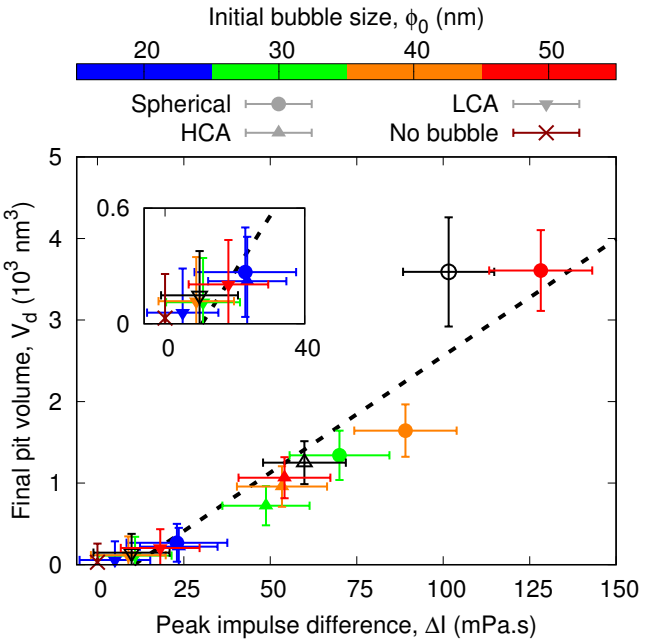

Fig. 11 Variation in surface damage volume V_d (from Equation (10)) with peak impulse difference ΔI, as measured at the impact centre. The different symbols and colours denote the bubble type and size, respectively, as shown in the legend. The empty black symbols refer to the 40 nm diameter vapour bubble cases. The straight line shows the line of best fit.

turbed substrate (see Figure 9(a)). Equation (10) describes the volume of material displaced from the mean undamaged reference line $z_{Si,0}$, which allows us to compare the pit volumes across all cases, since we were not able to fit a common shape to the surface nanobubble pits.

We observe a linear relationship between damage volume and peak impulse difference, shown by the fitted dashed line in Figure 11. All spherical cases above $\phi_0 \geq 30\,\text{nm}$ exceeded the peak impulse difference, and likewise pit volume, of all of the surface nanobubble cases. This increased peak impulse, as previously discussed, resulted from the higher jet velocities, as well as the concentrated and sustained pressures during jet impact and outward flow.

There were large differences in the surface damage volume between the 40 nm spherical vapour and gas-filled bubble cases, which were also seen in the pit depth measurements (see Figure 9(f)). This can now be explained by the large increase in ΔI, which is attributed to the reduced jet deceleration in the vapour case, compared to that seen in the gas-filled bubbles. In contrast, the differences between the respective 40 nm vapour and gas-filled surface nanobubbles were not as significant, for either of the HCA or LCA cases. We also observe smaller variations in impulse (and damage volume) for the HCA and LCA case when compared to the spherical cases, which seems consistent with the observed constant pit depths in Figure 9(f). The peak impulses from the LCA surface nanobubbles were not much greater than from the no-bubble case, which could explain why little damage was observed for these bubbles.

We also expect the observed linear relationship between peak impulse and surface damage volume to be dependent on the solid material properties, with softer materials possibly showing a steeper gradient. This finding may be useful for qualitatively estimating which bubble parameters, such as size and stand-off, could be the most damaging for a particular driving impulse, without actually needing to resolve the solid response, for example in computational fluid dynamics simulations.

4 Conclusions

We have investigated the shock-induced collapse of surface nanobubbles of varying size (20–50 nm) and contact angle (40–80°) using molecular dynamics simulations, and compared the results to the collapse of spherical bubbles close to a solid substrate. We observed the typical jet formation during cavitation collapse in all nanobubble simulations, with the jets accelerating until they impacted the nearest surface, either the distal bubble surface for the spherical bubble cases, or the solid substrate for the surface nanobubbles. In the surface nanobubble cases, the jets would impact the solid substrate before they could reach the same high jet speeds as seen in the spherical simulations, due to their spherical cap shape, and with the lower contact angle cases generally yielding the slowest jets.

The "weaker" jets from the collapsing surface nanobubbles were characterised by lower velocities, wider and flatter leading profiles, and reduced local vorticity generated around the bubbles, which generally resulted in lower impact pressures. The impact pressures roughly increased with the incident jet velocity, however, we also observed other complex localised pressure phenomena, such as from the high Mach number jets, and shock-wave reflections and interference, that could only be predicted by a full numerical simulation.

All the bubble cases produced pitting damage, and we found that the pit perimeters scaled with the initial bubble diameters, consistent with previous investigations.[11,28] However, there were significant differences in the pit formation and final depth, resulting from the earlier jet development. For example, the jets from the spherical nanobubble cases all impacted the substrate at a concentrated point, due to their curved profiles; after impact, the residual jet flowed radially outwards across the substrate and back up into the bulk liquid, forming a toroidal rebounding bubble in the larger cases. We call this behaviour "punch and drag", corresponding to the initial jet impact (the punch), and then the vorticity driven surface shear stresses from the fluid flow over the substrate (the drag), which produced high-curvature, spherical cap shaped pits, with a well-defined sharp lip around their perimeter.

In contrast, the weaker jets from the surface nanobubbles only appeared to "punch" the substrate, more closely resembling a plane shock-wave reflection, due to their flatter jet profile, and with no outward flow or toroidal rebounding bubble observed after impact. Consequently, the pitting damage was generally reduced, and most importantly, we observed near constant pit depths, which were dependent only on the initial contact angle, and not the initial diameter, as was found for the spherical nanobubbles. The constant pit depths were also produced in the vapour surface nanobubble cases, and so we suggest this effect resulted from their spherical cap geometry, rather than any jet deceleration by the internal gas phase.

Surface nanobubble collapse appears to limit the underlying substrate damage, which might make them more suitable in advanced nanomaterial manufacturing, health and precision cleaning, or applications involving fragile materials, where pitting is to be carefully controlled. Moreover, the differences in the shapes of the pit formation found here might also be useful for researchers trying to identify either spherical or surface nanobubble collapse in their experiments.

We found an apparent linear relationship between total surface damage volume and peak impulse at the impact centre, and consistent for all bubble cases. This finding could be used in computational fluid dynamics simulations to estimate the relative damage capacity of different bubble parameters, such as size and stand-off, for a given pressure input, and without needing to model the solid response. We encourage further investigations into these impulse distributions and the relationship with the bubble's collapsing dynamics and resulting solid response. These simulations only considered pitting damage from a single bubble collapse, although we expect repeated collapse of surface nanobubbles would still cause fatigue failure, and could also be modelled in the future.

Conflicts of interest

There are no conflicts of interest to declare.

Acknowledgements

This work is supported in the UK by the Engineering and Physical Sciences Research Council (EPSRC) under grants EP/N016602/1 and EP/R007438/1. All Molecular Dynamics (MD) simulations were run on ARCHER and ARCHER2, the UK's national supercomputing service, funded by an EPSRC/ARCHER2 Pioneer Project.

Notes and references

1 C. E. Brennen, *Cavitation and Bubble Dynamics*, Cambridge University Press, 2013.
2 S. Brems, M. Hauptmann, E. Camerotto, A. Pacco, T.-G. Kim, X. Xu, K. Wostyn, P. Mertens and S. De Gendt, *ECS J. Solid State Sci. Technol.*, 2014, **3**, N3010–N3015.
3 M. Dular, T. Griessler-Bulc, I. Gutierrez-Aguirre, E. Heath, T. Kosjek, A. K. Klemenčič, M. Oder, M. Petkovšek, N. Rački, M. Ravnikar, A. Šarc, B. Širok, M. Zupanc, M. Žitnik and B. Kompare, *Ultrason. Sonochem.*, 2016, **29**, 577–588.
4 E. Y. Lukianova-Hleb, X. Ren, R. R. Sawant, X. Wu, V. P. Torchilin and D. O. Lapotko, *Nat. Med.*, 2014, **20**, 778–784.
5 E. Y. Lukianova-Hleb, Y.-S. Kim, I. Belatsarkouski, A. M. Gillenwater, B. E. O'Neill and D. O. Lapotko, *Nat. Nanotechnol.*, 2016, **11**, 525–532.
6 A. Delalande, S. Kotopoulis, M. Postema, P. Midoux and C. Pichon, *Gene*, 2013, **525**, 191–199.
7 K. Manmi and Q. Wang, *Ultrason. Sonochem.*, 2017, **36**, 427–436.
8 O. Supponen, D. Obreschkow, M. Tinguely, P. Kobel, N. Dorsaz and M. Farhat, *J. Fluid Mech.*, 2016, **802**, 263–293.
9 T. B. Benjamin and A. T. Ellis, *Philos. Trans. R. Soc., A*, 1966, **260**, 221–240.
10 I. Akhatov, O. Lindau, A. Topolnikov, R. Mettin, N. Vakhitova and W. Lauterborn, *Phys. Fluids*, 2001, **13**, 2805–2819.
11 A. Philipp and W. Lauterborn, *J. Fluid Mech.*, 1998, **361**, 75–116.
12 P. Koukouvinis, M. Gavaises, O. Supponen and M. Farhat, *Phys. Fluids*, 2016, **28**, 032110.
13 S. Zhang and J. H. Duncan, *Phys. Fluids*, 1994, **6**, 2352–2362.
14 J. R. Blake, D. M. Leppinen and Q. Wang, *Interface Focus*, 2015, **5**, 20150017.
15 M. Fivel, J.-P. Franc and S. C. Roy, *Interface Focus*, 2015, **5**, 20150013.
16 E. Johnsen and T. Colonius, *J. Fluid Mech.*, 2009, **629**, 231–262.
17 O. Supponen, D. Obreschkow, P. Kobel, M. Tinguely, N. Dorsaz and M. Farhat, *Phys. Rev. Fluids*, 2017, **2**, 093601.
18 Y. Tomita and A. Shima, *J. Fluid Mech.*, 1986, **169**, 535–564.
19 J. Dzubiella, *J. Chem. Phys.*, 2007, **126**, 194504.
20 R. Hołyst, M. Litniewski and P. Garstecki, *Phys. Rev. E*, 2010, **82**, 066309.

21 J. Lombard, T. Biben and S. Merabia, *Phys. Rev. Lett.*, 2014, **112**, 105701.

22 U. Adhikari, A. Goliaei and M. L. Berkowitz, *J. Phys. Chem. B*, 2015, **119**, 6225–6234.

23 A. Stukowski, *Modell. Simul. Mater. Sci. Eng.*, 2010, **18**, 015012.

24 U. Adhikari, A. Goliaei and M. L. Berkowitz, *Phys. Chem. Chem. Phys.*, 2016, **18**, 32638–32652.

25 M. Vedadi, A. Choubey, K. Nomura, R. K. Kalia, A. Nakano, P. Vashishta and A. C. T. van Duin, *Phys. Rev. Lett.*, 2010, **105**, 014503.

26 A. Choubey, M. Vedadi, K.-I. Nomura, R. K. Kalia, A. Nakano and P. Vashishta, *Appl. Phys. Lett.*, 2011, **98**, 023701.

27 F. Magaletti, M. Gallo, L. Marino and C. M. Casciola, *Int. J. Multiphase Flow*, 2016, **84**, 34–45.

28 A. Shekhar, K.-I. Nomura, R. K. Kalia, A. Nakano and P. Vashishta, *Phys. Rev. Lett.*, 2013, **111**, 184503.

29 K. Nomura, R. K. Kalia, A. Nakano, P. Vashishta and A. C. T. van Duin, *Appl. Phys. Lett.*, 2012, **101**, 073108.

30 S. H. Min, S. Wijesinghe, E. Y. Lau and M. L. Berkowitz, *J. Phys. Chem. B*, 2020, **124**, 7494–7499.

31 J. Goeller, A. Wardlaw, D. Treichler, J. O'Bruba and G. Weiss, *J. Neurotrauma*, 2012, **29**, 1970–1981.

32 N. Ishida, T. Inoue, M. Miyahara and K. Higashitani, *Langmuir*, 2000, **16**, 6377–6380.

33 X. H. Zhang, A. Quinn and W. A. Ducker, *Langmuir*, 2008, **24**, 4756–4764.

34 Y. Liu and X. Zhang, *J. Chem. Phys.*, 2013, **138**, 014706.

35 H. An, G. Liu, R. Atkin and V. S. J. Craig, *ACS Nano*, 2015, **9**, 7596–7607.

36 D. Lohse and X. Zhang, *Phys. Rev. E*, 2015, **91**, 031003.

37 T.-W. Huang, S.-Y. Liu, Y.-J. Chuang, H.-Y. Hsieh, C.-Y. Tsai, W.-J. Wu, C.-T. Tsai, U. Mirsaidov, P. Matsudaira, C.-S. Chang, F.-G. Tseng and F.-R. Chen, *Soft Matter*, 2013, **9**, 8856–8861.

38 V. S. J. Craig, *Soft Matter*, 2011, **7**, 40–48.

39 D. Lohse and X. Zhang, *Rev. Mod. Phys.*, 2015, **87**, 981–1035.

40 P. E. Theodorakis and Z. Che, *Adv. Colloid Interface Sci.*, 2019, **272**, 101995.

41 A. Andersen and K. A. Mørch, *J. Fluid Mech.*, 2015, **771**, 424–448.

42 D. Dockar, M. K. Borg and J. M. Reese, *Langmuir*, 2019, **35**, 9325–9333.

43 V. Belova, M. Krasowska, D. Wang, J. Ralston, D. G. Shchukin and H. Möhwald, *Chem. Sci.*, 2013, **4**, 248–256.

44 D. Dockar, L. Gibelli and M. K. Borg, *J. Chem. Phys.*, 2020, **153**, 184705.

45 C. U. Chan, M. Arora and C.-D. Ohl, *Langmuir*, 2015, **31**, 7041–7046.

46 P. Attard, *Langmuir*, 2016, **32**, 11138–11146.

47 X. Zhu, R. Verzicco, X. Zhang and D. Lohse, *Soft Matter*, 2018, **14**, 2006–2014.

48 Z. Guo, X. Wang and X. Zhang, *Langmuir*, 2019, **35**, 8482–8489.

49 D. S. Bull, N. Nelson, D. Konetski, C. N. Bowman, D. K. Schwartz and A. P. Goodwin, *J. Phys. Chem. Lett.*, 2018, **9**, 4239–4244.

50 Y.-X. Chen, Y.-L. Chen and T.-H. Yen, *Langmuir*, 2018, **34**, 15360–15369.

51 J. R. T. Seddon, D. Lohse, W. A. Ducker and V. S. J. Craig, *ChemPhysChem*, 2012, **13**, 2179–2187.

52 B. H. Tan, H. An and C.-D. Ohl, *Curr. Opin. Colloid Interface Sci.*, 2021, **53**, 101428.

53 A. J. Jadhav and M. Barigou, *Langmuir*, 2020, **36**, 1699–1708.

54 A. Agarwal, W. J. Ng and Y. Liu, *Chemosphere*, 2011, **84**, 1175–1180.

55 G. L. Chahine and C.-T. Hsiao, *Interface Focus*, 2015, **5**, 20150016.

56 S. Cao, G. Wang, O. Coutier-Delgosha and K. Wang, *J. Fluid Mech.*, 2021, **907**, A17.

57 S. Plimpton, *J. Comput. Phys.*, 1995, **117**, 1–19.

58 V. Molinero and E. B. Moore, *J. Phys. Chem. B*, 2009, **113**, 4008–4016.

59 B. Coasne, A. Galarneau, F. Di Renzo and R. J. M. Pellenq, *Langmuir*, 2010, **26**, 10872–10881.

60 R. L. C. Vink, G. T. Barkema, W. F. van der Weg and N. Mousseau, *J. Non-Cryst. Solids*, 2001, **282**, 248–255.

61 F.-C. Wang and H.-A. Wu, *Soft Matter*, 2013, **9**, 5703–5709.

62 F. H. Stillinger and T. A. Weber, *Phys. Rev. B*, 1985, **31**, 5262–5271.

63 W. G. Hoover, *Phys. Rev. A*, 1985, **31**, 1695–1697.

64 S. Nosé, *J. Chem. Phys.*, 1984, **81**, 511–519.

65 Y. C. Huang, F. G. Hammitt and T. M. Mitchell, *J. Appl. Phys.*, 1973, **44**, 1868–1869.

66 F. J. Heymann, *J. Appl. Phys.*, 1969, **40**, 5113–5122.

67 S. H. Min and M. L. Berkowitz, *J. Chem. Phys.*, 2018, **148**, 144504.

68 E. W. Lemmon, M. O. McLinden and D. G. Friend, *NIST Chemistry WebBook, NIST Standard Reference Database Number 69, Eds. P.J. Linstrom and W.G. Mallard*, National Institute of Standards and Technology, Gaithersburg, 20899, 2017.

69 L. E. Kinsler, A. R. Frey, A. B. Coppens and J. V. Sanders, *Fundamentals of acoustics*, John Wiley & Sons, 1999.

70 L. Rayleigh, *London, Edinburgh Dublin Philos. Mag. J. Sci.*, 1917, **34**, 94–98.

71 M. S. Plesset, *J. Appl. Mech.*, 1949, **16**, 277–282.

72 A. Kapahi, C.-T. Hsiao and G. L. Chahine, *J. Phys.: Conf. Ser.*, 2015, **656**, 012128.

73 J. B. Keller and M. Miksis, *J. Acoust. Soc. Am.*, 1980, **68**, 628–633.

74 J. P. Dear and J. E. Field, *J. Appl. Phys.*, 1988, **63**, 1015–1021.

75 F. G. Blake, Jr., *Onset of Cavitation in Liquids: I*, Acoustics Research Laboratory, Harvard University Technical Memorandum 12, 1949.

76 T. Kodama, M. R. Hamblin and A. G. Doukas, *Biophys. J.*, 2000, **79**, 1821–1832.